

Experimental PET imaging

The limitation of PET imaging for biological adaptive-IMRT assessed in animal models

Nicolas Christian^a, John A. Lee^a, Anne Bol^a, Marc De Bast^a, B. Jordan^b, Vincent Grégoire^{a,c,*}^a Center for Molecular Imaging and Experimental Radiotherapy, Université Catholique de Louvain, Brussels, Belgium^b Biomedical Magnetic Resonance Unit, Université Catholique de Louvain, Brussels, Belgium^c Department of Radiation Oncology, Cliniques Universitaires St. Luc, Brussels, Belgium

ARTICLE INFO

Article history:

Received 22 May 2008

Received in revised form 13 October 2008

Accepted 14 November 2008

Available online 26 December 2008

Keywords:

Mouse tumor

Animal PET

Autoradiography

Image-guided radiotherapy

FDG

Molecular imaging

ABSTRACT

Purpose: Biological image-guided radiotherapy aims at specifically irradiating biologically relevant sub-volumes within the tumor, as determined for instance by PET imaging. This approach requires that PET imaging be sensitive and specific enough to image various biological pathways of interest, e.g. tumor metabolism, proliferation and hypoxia. In this framework, a validation of PET imaging used for adaptive radiotherapy was undertaken in animal models by comparing small-animal PET images (2.7 mm resolution) with autoradiography (AR) (100 μ m resolution) in various tumors under various physiological situations.

Methods: A specific template for tumor-bearing mouse imaging has been designed (Christian, R&O, 2008). It allows for the registration between MRI images (Biospec, Bruker), FDG-PET images (Mosaic, Philips) and AR (FLA-5100, Fujifilm). After registration, the tumors on the PET and AR images were segmented using a threshold-based method. The thresholds were selected to obtain absolute equal volumes in the PET and AR images. Matching indexes were then calculated between the various volumes. The entire imaging process was performed for FSaII tumors ($n = 5$), SCCVII ($n = 5$) and irradiated (35 Gy) FSaII tumors ($n = 5$).

Results: In regions with high FDG activity delineated using high value thresholds, low matching values of $39\% \pm 11\%$ (mean \pm SD) were observed between the volumes delineated on the PET images and those delineated on AR. The matching values progressively increased when considering larger volumes obtained with lower thresholds. These findings were independent of tumor type, tumor metabolism or tumor size. The relationship between the matching values and the percentage of overall tumor volume was fitted through a power regression ($r = 0.93$). As shown by simulations, the matching improved with higher PET resolution. The results can be extrapolated to human tumors imaged with a whole-body PET system.

Conclusion: Discrepancies were found between the PET images and the underlying microscopic reality represented by AR images. These differences, attributed to the finite resolution of PET, were important when considering small and highly active regions of the tumors. Dose painting based on PET images should therefore be carefully considered and should take these limitations into account.

© 2008 Elsevier Ireland Ltd. All rights reserved. Radiotherapy and Oncology 91 (2009) 101–106

Biological image-guided intensity modulated radiotherapy (BIG-IMRT) aims at specifically irradiating biologically relevant sub-volumes within a tumor. Due to the heterogeneous pattern of tumors at the microscopic level [1], the delivery of a uniform dose distribution is a coarse simplification of reality. By sculpting the dose on particular regions identified with functional imaging, this approach intends to specifically increase the prescribed dose, thus potentially increasing cell kill and hopefully enhancing tumor control rate. This approach is also supported by the fact that a

homogeneous dose escalation on large volumes might be limited by radiation-induced toxicity on the surrounding normal tissues and/or on the normal tissues embedded in the planning target volumes (PTVs) [2,3].

In this framework, positron emission tomography (PET) combined with various tracers may provide insight into various biological pathways of importance in response to ionizing radiation, such as proliferation, hypoxia, or cell metabolism [4,5]. PET-positive volumes inside a tumor might then be used to “sculpt” (or paint) the dose using IMRT. Different studies have shown the feasibility of dose-painting based on PET images [6,7]. Most of them used [18 F]FDG, but studies with hypoxia tracers have also been reported [8,9]. In the above-mentioned studies, the dose

* Corresponding author. Address: Department of Radiation Oncology, Cliniques Universitaires Saint-Luc, Avenue Hippocrate, 10, B-1200 Brussels, Belgium.

E-mail address: vincent.gregoire@uclouvain.be (V. Grégoire).

was escalated homogeneously on the PET sub-volumes, but another approach was proposed whereby the dose is escalated based on the PET voxel intensity values [10]. Preliminary clinical data have already been reported for head and neck squamous cell carcinoma [11]. These studies rely on the fact that there is a perfect correlation between the detection of the PET signal and the underlying biology of interest. However, despite improvements in PET instrumentation, data processing and image reconstruction algorithms, the resolution and sensitivity of PET systems are still limiting factors leading to artifacts such as partial volume effect (PVE) [12]. As a consequence, and despite the widespread use of clinical studies on dose escalation, uncertainties still remain about the level of correlation between the *in vivo* images and the underlying biological phenomena at the molecular level.

The validation of the use of functional imaging for BIG-IMRT thus requires a direct comparison between *in vivo* and *ex vivo* imaging modalities. For *ex vivo* imaging, autoradiography (AR) will allow the closest visualization at the cellular level of the tracer's distribution. As far as the tumor model is concerned, due to the relatively short half-life of ^{18}F labeled tracers (109.8 min) and the time required to process human tumors after surgical resection, mouse tumors imaged with an animal PET do represent better models.

In the present study, we report on the correlation between FDG distribution in mouse tumors assessed *in vivo* with an animal-PET and *ex vivo* by AR on tumor sections.

Materials and methods

Animal and tumor model

Seven- to 12-week-old male C3H/HeOulJo (IFFA Credo Belgium) mice were used for this study. Animals were maintained in a facility approved by the Belgian Ministry of Agriculture in accordance with current regulations and standards. They were housed 4–5 per cage and fed *ad libitum*. FSA II fibrosarcoma or SCCVII squamous cell carcinoma syngeneic to C3Hf/Kam mice was generated in the right thigh. These tumors were kindly provided by Dr. L. Milas from the University of Texas, M.D. Anderson Cancer Center, Houston, USA. Maintenance and expansion were done as previously described [13]. Tumor growth was determined by daily measurements of the three orthogonal diameters with a caliper. All the experiments were approved by the Ethics Committee on the animal experimentation of the medical school of the Université Catholique de Louvain. The “Principles of laboratory animal care” (NIH Publication No. 86-23, revised 1985) were strictly followed.

Fifteen tumor-bearing mice underwent the whole imaging process and were divided into three groups: FSAII ($n = 5$), SCCVII ($n = 5$) and irradiated FSAII tumors ($n = 5$). FSAII and SCCVII tumors were imaged when the tumors had reached 10–12 mm in diameter. In the irradiated FSAII group (FSAII + RX), a first [^{18}F]FDG-PET image was acquired when the tumors had reached 10–11 mm. On the same day, tumors were locally irradiated with 35 Gy of 250 kV X-rays (RT 250, Philips Medical System, 0.92 Gy/min) using a 3 cm-diameter circular irradiation field. The whole imaging process (MRI, PET, autoradiography) was carried out 6 ($n = 3$) or 7 ($n = 2$) days after irradiation.

During the whole procedure (immobilization, MRI imaging, PET imaging or irradiation) until euthanasia, the mice were kept anesthetized with an *i.p.* injection of 80 mg/kg of ketamine (Ketalar®, Parke-Davis, Warner Lambert S.A., Belgium) and 8 mg/kg of xylazine (Rompun®, Bayer AG, Germany). The time in the immobilization device was kept as short as possible.

In vivo imaging

Mice were kept anesthetized in a specifically designed immobilization device for the whole imaging procedure. Details about the device and the image registration accuracy have already been published [14]. First, MRI images were acquired on a 4.7 T (200 MHz, 1 H), 40 cm inner diameter bore system (Bruker Biospec, Ettlingen, Germany). T2-weighted images were obtained using a fast spin echo sequence (repetition time = 4.7, echo time = 12 ms, N averages = 8, RARE factor = 8). The total acquisition time was, on average, 10 min. A birdcage radiofrequency coil with an inner diameter of 60 mm was used for radiofrequency transmission and reception. Axial images were acquired using a matrix of $128 \times 128 \times 40$, with a voxel size of $0.508 \times 0.508 \times 1.0 \text{ mm}^3$. After MRI, mice were injected with 11.1 MBq (300 μCi) of [^{18}F]FDG through the tail vein. One hour later, a 15 min static PET acquisition was performed on a dedicated small-animal PET scanner (Mosaic®, Philips Medical Systems, Cleveland) with an in-plane spatial resolution of 2.7 mm (full width at half maximum, FWHM) [15]. A transmission scan was then obtained (with correction for emission contamination) in a single mode using a 370 MBq ^{137}Cs source for attenuation correction. All images were reconstructed with a full-3D iterative algorithm (3D-RAMLA) in a $128 \times 128 \times 120$ matrix, with a voxel size of 1 mm^3 .

Ex vivo imaging

Immediately after PET imaging, the anesthetized mouse was euthanized with a lethal dose of pentobarbital (200 mg/kg) injected *s.c.* in the neck. The whole set (mouse and its immobilization device) was then frozen at -25°C for 5 h and was then sliced (Universal slicer MA9101, Bosch, Germany), perpendicular to the longitudinal axis. The thickness of each slice was measured with a caliper, and the slices were then exposed at -25°C for 45 min to a phosphor storage plate (BAS-MS 2025, Fuji Photo Film Co., Japan). The ^{18}F distribution image was then digitalized using a fluorescent image analyzer (FLA-5100, Fuji Photo Film Co., Japan) with a scan resolution of 100 μm .

Image analysis was performed as already described [14]. Briefly, the image file containing the ^{18}F distribution of all slices was imported in a home made software for 3D reconstruction. All slices were stacked in the proper order and aligned. The voxel size of the resulting volume was 100 μm in both x and y directions; the average voxel axial size (z -direction) reached 1.10 mm for the 15 mice used for these experiments. An up-sampling process in the z -direction was performed. The slice thickness was decreased by a twofold factor, and intermediate slices were interpolated between each of the slices obtained from autoradiography.

Image analysis and statistical evaluation

The PET and MRI images were then registered with 3D autoradiography (AR) images (3DAR, PMod Technologies Ltd., Switzerland), the latter being selected as the reference images. After registration, all images acquired the voxel size of the reference images (i.e. $0.1 \times 0.1 \times \sim 0.55 \text{ mm}$). The tumors were then manually delineated on the registered MRI images, and the volumes were transferred on the registered 3DAR and PET images.

In addition, an artificial PET-like image was created by blurring the 3DAR with a 3D 2.7 mm FWHM Gaussian function in order to simulate the resolution of the PET system. The voxel size of this blurred image was increased up to 1 mm^3 so as to correspond to the voxel size of the Mosaic PET image. This image was called 3D blurred autoradiography image (blurred-3DAR).

The PET and 3DAR images were then segmented using a threshold-based method. The volumes segmented on the PET

images were transferred to the 3DAR images. The segmented volumes (volumes A and B in PET and 3DAR images, respectively) were then compared, and the matching between these images was calculated using the dice similarity index (DSI) defined as [16]

$$DSI = \frac{2|A \cap B|}{|A| + |B|} \quad (1)$$

In this study, the volumes A and B were always chosen to be equal. In consequence, DSI values can be read as the percentage of volume that is common to A and B.

The linearity of both imaging devices has been tested in a range of activity between 30 and 350 kBq/ml, thus including the typical activity found in a mouse tumor at the time of acquisition (185 kBq/ml for PET imaging and 30 kBq/ml for autoradiography).

Data were analyzed with NCSS 2005 (Number Crunch Statistical System, Kaysville, USA) using an alpha level of significance of 0.05.

Results

Tumor models

For the 15 mice used in these experiments, the mean tumor volume assessed on MRI images reached 1.65 ± 0.49 ml. In the three different groups, the mean volumes were 1.50 ± 0.49 , 1.72 ± 0.39 and 1.86 ± 0.62 ml for the FSaII tumors, SCCVII tumors and FSaII + RX tumors, respectively. Tumor volume was not significantly different between the groups (one-way ANOVA: $p = 0.53$). The smaller tumor reached 0.92 ml (FSaII group) and the larger tumor reached 2.70 ml (FSaII + RX group).

Voxel-by-voxel analysis

After registration, the tumor was manually delineated on the MRI images, and the volumes were transferred to the blurred-3DAR and to the native PET images. Within the tumor volume, a voxel intensity-by-voxel intensity analysis was performed between the native PET images and the downsized blurred images (Fig. 1). The mean determination coefficients r^2 (\pm SD) were 0.83 ± 0.03 , 0.86 ± 0.07 and 0.88 ± 0.04 for the FSaII, the SCCVII and the FSaII + RX tumors, respectively. These results illustrate the good spatial correlation between the native PET images and the blurred-3DAR images. Another comparison was made between the high resolution 3DAR and the original PET images after registration and trilinear interpolation. The mean determination coefficient r^2 (\pm SD) reached 0.88 ± 0.03 , 0.89 ± 0.02 and 0.85 ± 0.04 for the FSaII, the SCCVII and the FSaII + RX tumors, respectively.

Matching analysis

Tumor volumes were delineated on MRI images and then transferred to the 3DAR and to the PET images. A threshold-based segmentation was then applied on these modalities to automatically delineate regions of given activities. The thresholds were selected to obtain volumes corresponding to 5%, 10%, 20%, 30%, 40%, 50%, 60%, 70%, 80%, 90% and 100% of the overall tumor volume delineated on MRI.

The matching between the AR and PET images was analyzed using the DSI for various thresholds of segmentation (Fig. 2). The results were not significantly different between the three groups of tumors/treatment (repeated measures ANOVA: $p = 0.429$). A curve was thus fitted through the points using power regression ($r^2 = 0.83$) with the equation:

$$DSI = (\text{Percentage of vol.})^a \quad (2)$$

where a is equal to 0.291. The choice of regression model is guided by the fact that it agrees with the intuition that the DSI for 0% of the volume is zero and the DSI for 100% of the volume is 100%.

For small fractions of tumor volumes (i.e. 5–10%), i.e. the voxels with the highest FDG activity, mean DSI values were close to 40–50%. In other words, when considering such small sub-volumes on the PET images, around half of the voxels with high FDG activity were not included (Fig. 3). Moreover, for such small fractions, the DSI variability was important.

The relationship between DSI and fractional volume was independent of the tumor size. Indeed, no significant difference in DSI was observed between tumor volumes below and above the median volume (repeated measures ANOVA $p = 0.157$). Moreover, when plotting the DSI for various fractions of tumor volume (i.e. 5%, 10% and 20%) versus the overall tumor volume, no relationship was found. The r^2 coefficient never exceeded 0.23, a value obtained for the 5% fraction.

Effect of resolution

The initial FWHM of the Gaussian function, convolved with the 3DAR to obtain the blurred-3DAR, was 2.7 mm, which corresponds to the spatial resolution of the Mosaic PET scanner. By changing the size of the FWHM, i.e. by blurring more or less the images, it was possible to simulate the effect of the scanner resolution on the matching results. In other words, with a smaller FWHM, the resulting blurred-3DAR simulates images were acquired with a scanner of higher resolution, and conversely. The whole data set of 3DAR images ($n = 15$) was convolved with Gaussian functions of 1.5, 2.0, 2.5, 2.7, 3.0 and 3.5 mm FWHM. The same segmentation process was then applied, and the corresponding volumes were compared between 3DAR and blurred-3DAR (Fig. 4). As expected, there

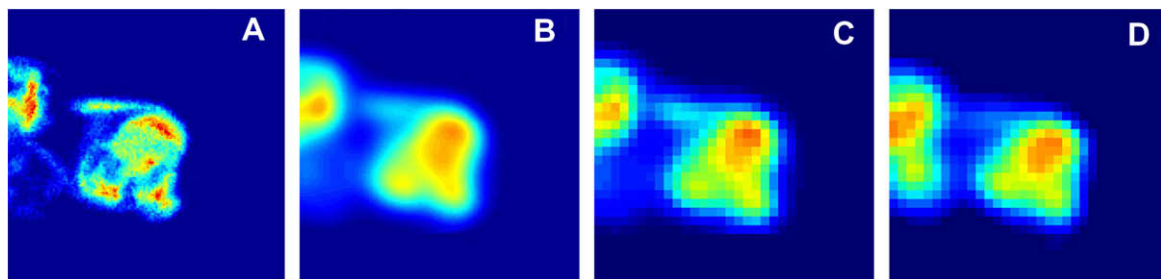


Fig. 1. From left to right: (A) autoradiography (transversal view) of a 11 mm diameter FSaII tumor; (B) this image was blurred with a 2.7 mm FWHM 3D Gaussian function; (C) the voxel size was increased up to 1 mm^3 ; (D) native PET image. The hot spot at the left side of the PET image, which is not visible on the AR image, corresponds to the bladder activity. This region was manually removed from the slice during processing since it could potentially generate artifacts, i.e. urine tends to warm up during slicing and spread to the whole section.

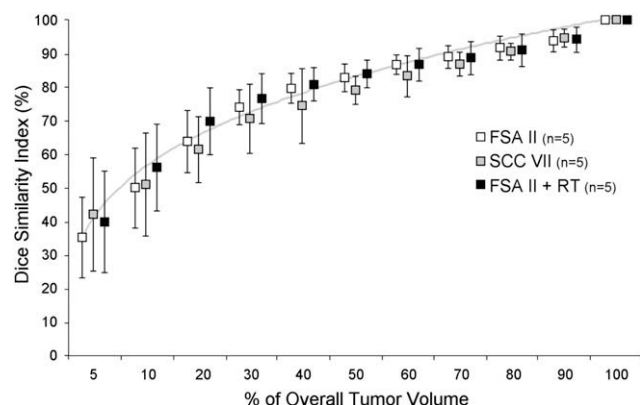


Fig. 2. Mean dice similarity index between the autoradiography and the PET images for different percentages of overall tumor volume: white squares FSAII ($n = 5$), grey squares SCCVII ($n = 5$), black squares FSAII + RX ($n = 5$). Differences between groups were not significant (repeated measures ANOVA: $p = 0.43$). The grey line is the power regression curve for the whole data set ($y = x^{0.291}$).

was an increase in DSI with the improvement of the PET resolution. For the 5% sub-volumes, the DSI increased by more than 25% when the FWHM was reduced from 3.5 to 1.5 mm. However, even with such relatively high-resolution images, DSI never exceeded 70%, meaning that still a non-negligible percentage of high activity voxels remained undetected at that resolution.

Power regression curves kept the same general expression (see Eq. (2)), where a increases with the FWHM of the Gaussian function (Fig. 5). These results show that the influence of the image resolution on the matching between AR and PET images is predictable, and could thus be extrapolated to other PET cameras with different image resolutions.

Discussion

Our study demonstrated that sub-volumes of mouse tumors with high FDG-PET activity, which likely represent the regions where radiation dose might be escalated, poorly matched with the underlying reality assessed by autoradiography (Fig. 3). It was also shown that these results could be extrapolated to human tumors imaged with a whole-body PET camera. Last, it was shown that the use of PET camera with a higher resolution would definitely improve the whole scenario (Fig. 4).

We established that the relationship between the DSI (expressing the matching between PET and autoradiography images) and the percentage of tumor volume taken into account could be fitted by a power curve. This relationship was independent of the tumor type, and was not altered by changes in tumor metabolism, as in-

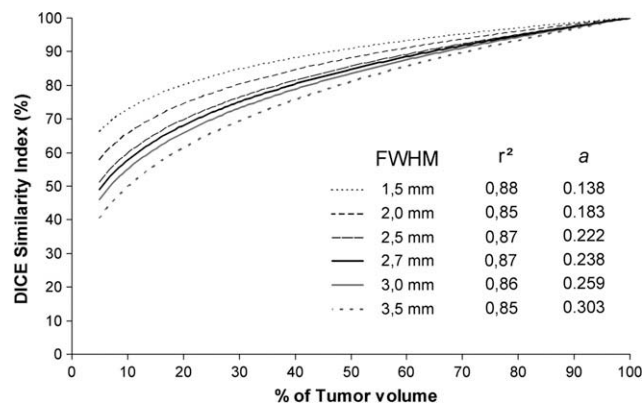


Fig. 4. Influence of spatial resolution on the relationship between dice similarity index and fractional volume. Various spatial resolution images were obtained by modifying the FWHM when blurring the 3D-autoradiography with Gaussian functions. These various blurred 3D-autoradiographies were matched with the native AR images for various fractional tumor volumes. All regression curves were fitted with the same general equation defined as $DSI = (\% \text{ of tum. vol.})^a$, where a varies as a function of the FWHM.

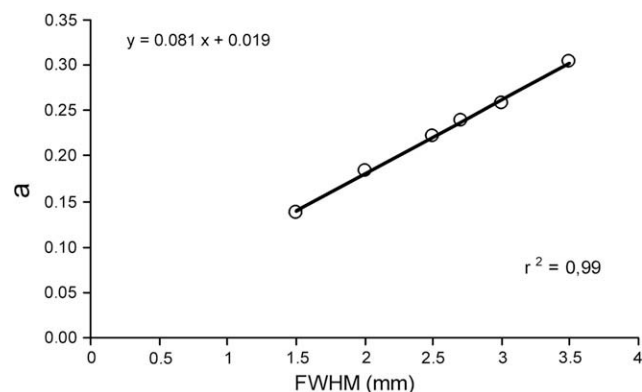


Fig. 5. Correlation between the exponent " a " and the FWHM of the Gaussian functions for the different regression curves (see Fig. 4).

duced by the local irradiation. In other words, this observation appears to be more related to the technical limitation of the PET camera than to the biological artifacts. This observation is likely a specific expression of the finite resolution effects, which affect all PET images. The limited spatial resolution of this imaging modality is usually characterized by the full width at half maximum (FWHM) of the spread function (point spread function or line spread function), and produces a blurring effect which is responsible for the well-known partial volume effect (PVE). PVE leads to

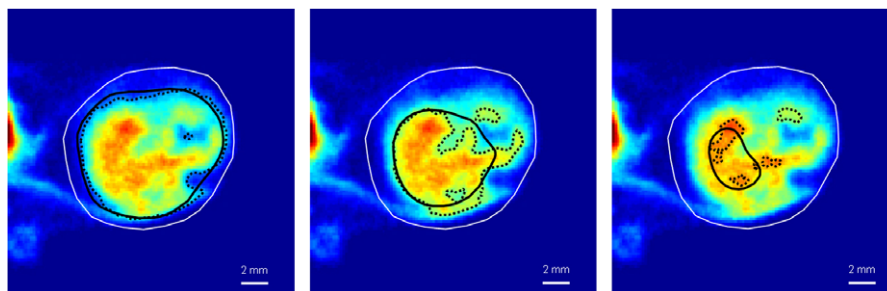


Fig. 3. Autoradiography images of a 12 mm diameter FSAII tumor transversal section. The volume delineated by threshold-based segmentation on the autoradiography (AR) image is represented by the dotted lines, whereas the volume segmented on the corresponding PET image is represented by the bold line. The external contour (white) has been delineated on the MRI and corresponds to the entire anatomic tumor volume. For both AR and PET, the sub-volumes correspond to 80%, 40% and 10% of the full tumor volume of 2.01 ml. The dice similarity index was 0.94, 0.76 and 0.38, respectively.

quantification errors in PET images by producing an underestimation of the activity concentrations in objects which are smaller than twice to three times the FWHM of the resolution function, and by inducing an overestimation in structures that are adjacent to the high activity concentration regions (spillover effect). Actually, PVE is often incriminated when PET is used as a staging tool, but its effect on quantitative SUV values can be estimated by taking into account the size of the object and the FWHM of the system resolution [19]. Most methods developed for PVE correction rely on simplified assumptions and only work for isolated homogeneous spots in a uniform background [12].

Finite resolution effects become an important limitation when PET is used as a functional intratumoral mapping tool since, in this application, the sub-volumes within the tumor are likely smaller than the FWHM of the camera. The high activity sub-volumes within a tumor only have a functional reality with no definite anatomical boundaries. Precise measurement of their size is therefore not feasible. A finite resolution correction in this setting must be more elaborate. The existing simplified PVE correction methods cannot deal with highly heterogeneous regions. Deconvolution algorithms [12], which may potentially lessen the PVE, are also inapplicable due to the high heterogeneity in activity concentration within the tumors. The only theoretical solution to improve the matching between the PET camera and the underlying reality is to use higher resolution devices or to apply resolution recovery techniques during image reconstruction to include resolution effects [20].

The conclusions drawn from our data rely, to a significant extent, on the robustness of the experimental conditions used in the present experiments and, in particular, on the registration between the 3DAR and the PET images. Despite the high accuracy observed in this registration process, a small misalignment could not be ruled out, which could explain the rapid drop in DSI, especially for small sub-volumes, e.g. 5–10%. Moreover, tumor processing (freezing, slicing and reconstruction) may have introduced several artifacts in the 3DAR images. The results obtained after 3DAR and PET images analysis were therefore compared to the data obtained after 3DAR and blurred-3DAR comparison. For the latter pair of images, registration is obviously perfect. Regardless of the artifacts that are induced, we could consider the 3D assembled autoradiography images as the *real* images, and then observe the effects of PET imaging simply by blurring them with a 3D Gaussian filter. As in the former case, the same relationship between the DSI and the volume fraction was found, except that it led to a slightly lower value of α , i.e. higher DSI values. In practice, this results in a maximal difference of 7% for the 5% sub-volume fraction, which illustrates that a misalignment between AR and PET images could not explain the mismatch observed between 3DAR and PET images. Moreover, the effect of a small misalignment between images was also evaluated. After a comparison between 3DAR and perfectly aligned corresponding blurred-3DAR, a small misalignment was introduced, corresponding to the mean registration error described in [14]. When this error was introduced, the mean DSI curve obtained after comparison was lower than the initial curve, with a mean maximal difference of 5% observed for the 5% overall volume comparison ($n = 5$).

Another interesting observation is the lack of correlation between DSI and tumor volume. It would be intuitive to expect better matching indices for larger tumors, since the PVE is a volume-related effect. In our study, high DSI values were also observed for smaller tumors. After careful visual examination of the images, it became obvious that the key factor influencing the correlation between PET images and microscopic tracer distribution was not the volume of the tumor itself but rather the volume of the hot spots visualized in autoradiography. Even in large tumors, small high activity regions, scattered everywhere in the tumor, lead to a low

DSI, while large homogeneous activity regions increased the DSI even for small tumors. Irradiation was also believed to have an impact on the results, by profoundly modifying the metabolism of tumors and FDG uptake. After resetting the metabolism, one could think that tumor regrowth may arise from a particular and isolated region, corresponding to an individual FDG hotspot, with high correlation between PET images and autoradiography. As observed, irradiation has no influence of the accuracy of PET imaging for detecting the true microscopic tracer uptake.

An important step for the clinical use of BIG-IMRT is to assess how the animal data presented above would apply to clinical situations with larger tumors but also lower resolution PET camera. It may well be that larger objects imaged on a lower resolution system give the same relative image quality than smaller object on a higher resolution machine. Such extrapolation to human devices could be achieved by using the ratio between the FWHM and the diameter of the tumors.

In the present study, the mean tumor volume was 1.65 ml. For spheres, which is a reasonably good approximation for these tumors, the corresponding diameter would be 14.7 mm. Imaged on the Mosaic PET camera (FWHM of 2.7 mm), such tumors would correspond to a FWHM-diameter ratio of 0.184. The typical resolution of modern clinical PET cameras is around 5.5 mm [17,18]. Using a FWHM-diameter ratio of 0.184 and a FWHM of 5.5 mm, the corresponding tumor diameter would be 29.9 mm, which is equivalent to a sphere of 14 ml. In other words, imaging a 1.65 ml sphere in a 2.7 mm FWHM resolution PET camera would be comparable to imaging a 14 ml sphere in a human PET.

In the present study, the experimental data were obtained for tumor volumes ranging from 0.92 to 2.70 ml. After transposition to a human situation, these volumes would correspond to spheres between 8 and 23 ml, respectively. By using such model, our animal data could be extrapolated to human tumor volumes ranging from 8 to 23 ml. Such volumes are typically observed for pharyngo-laryngeal tumors treated by radiotherapy [21,22]. However, this extrapolation, based on the FWHM-tumor diameter ratio, assumed spherical tumors with uniform FDG activity, which is obviously an oversimplification of the reality. Tumors are highly heterogeneous and have complex relationships with the host-tissue, in which they are developed [23]. Therefore, assuming an exact similarity between a mouse tumor model and human tumors and their heterogeneities is, again, a risky shortcut. However, the differences in resolution between the cellular level in human tumor and PET imaging is undeniable, and is most probably in the same range than those observed in our animal model. In consequence, even if these equations may not exactly depict the correlation between human PET and the human microscopic level, such relationship should also be present for human tumors. Furthermore, our images were obtained in anaesthetized, thus perfectly immobile, mice whereas human PET acquisitions are performed in free-breathing patients. Any movement during the acquisition is likely to degrade the spatial resolution of the camera, thus further decreasing the correlation between the microscopic and macroscopic images.

In conclusion, discrepancies were found between the *in vivo* PET images and the underlying microscopic reality. These differences were particularly important in small highly active regions of the tumors. Dose painting based on FDG–PET voxel intensity should therefore be carefully considered, and thus requires further evaluation before widespread clinical use.

Acknowledgments

Nicolas Christian is a research fellow of the “Fonds pour la formation à la Recherche dans l’Industrie et l’Agriculture (F.R.I.A.)” of Belgium. The project was supported by a grant from the “Fonds

Joseph Maisin”, Brussels, Belgium, by the European Commission’s Sixth Framework Programme funding (Contract N°. LSHC-CT-2004-505785), and by a program project from the “Institut National du Cancer” of France (Project INCa N° RS 020).

References

- [1] Hoogsteen IJ, Marres HA, Bussink J, van der Kogel AJ, Kaanders JH. Tumor microenvironment in head and neck squamous cell carcinomas: predictive value and clinical relevance of hypoxic markers. A review. *Head Neck* 2007;29:591–604.
- [2] De Neve W, Duthoy W. Intensity-modulated radiation therapy for head and neck cancer. *Expert Rev Anticancer Ther* 2004;4:425–34.
- [3] Lauve A, Morris M, Schmidt-Ullrich R, Wu Q, Mohan R, Abayomi O, et al. Simultaneous integrated boost intensity-modulated radiotherapy for locally advanced head-and-neck squamous cell carcinomas: II. Clinical results. *Int J Radiat Oncol Biol Phys* 2004;60:374–87.
- [4] Mahy P, Geets X, Lonnew M, Leveque P, Christian N, De Bast M, et al. Determination of tumour hypoxia with [¹⁸F]EF3 in patients with head and neck tumours: a phase I study to assess the tracer pharmacokinetics, biodistribution and metabolism. *Eur J Nucl Med Mol Imaging* 2008;35:1282–9.
- [5] Salskov A, Tammisetti VS, Grierson J, Vesselle H. FLT: measuring tumor cell proliferation in vivo with positron emission tomography and 3'-deoxy-3'-[¹⁸F]fluorothymidine. *Semin Nucl Med* 2007;37:429–39.
- [6] Chao KS, Bosch WR, Mutic S, Lewis JS, Dehdashti F, Mintun MA, et al. A novel approach to overcome hypoxic tumor resistance. Cu-ATSM-guided intensity-modulated radiation therapy. *Int J Radiat Oncol Biol Phys* 2001;49: 1171–82.
- [7] Douglas JG, Stelzer KJ, Mankoff DA, Tralins KS, Krohn KA, Muzi M, et al. [F-18]-Fluorodeoxyglucose positron emission tomography for targeting radiation dose escalation for patients with glioblastoma multiforme: clinical outcomes and patterns of failure. *Int J Radiat Oncol Biol Phys* 2006;64:886–91.
- [8] Grosu AL, Souvatzoglou M, Roper B, Dobritz M, Wiedenmann N, Jacob V, et al. Hypoxia imaging with FAZA-PET and theoretical considerations with regard to dose painting for individualization of radiotherapy in patients with head and neck cancer. *Int J Radiat Oncol Biol Phys* 2007;69:541–51.
- [9] Lee NY, Mechalakos JG, Nehmeh S, Lin Z, Squire OD, Cai S, et al. Fluorine-18-labeled fluoromisonidazole positron emission and computed tomography-guided intensity-modulated radiotherapy for head and neck cancer: a feasibility study. *Int J Radiat Oncol Biol Phys* 2007;70:2–13.
- [10] Bentzen SM. Theragnostic imaging for radiation oncology: dose-painting by numbers. *Lancet Oncol* 2005;6:112–27.
- [11] Vanderstraeten B, Duthoy W, De Gersem W, De Neve W, Thierens H. [¹⁸F]Fluoro-deoxy-glucose positron emission tomography ([¹⁸F]FDG-PET) voxel intensity-based intensity-modulated radiation therapy (IMRT) for head and neck cancer. *Radiother Oncol* 2006;79:249–58.
- [12] Soret M, Bacharach SL, Buvat I. Partial-volume effect in PET tumor imaging. *J Nucl Med* 2007;48:932–45.
- [13] Milas L, Hunter N, Mason K, Withers HR. Immunological resistance to pulmonary metastases in C3Hf-Bu mice bearing syngeneic fibrosarcoma of different sizes. *Cancer Res* 1974;34:61–71.
- [14] Christian N, Lee JA, Bol A, De Bast M, Gallez B, Grégoire V. Immobilization device for in vivo and in vitro multimodality image registration of rodent tumors. *Radiother Oncol* 2008;87:147–51.
- [15] Huisman MC, Reder S, Weber AW, Ziegler SI, Schwaiger M. Performance evaluation of the Philips MOSAIC small animal PET scanner. *Eur J Nucl Med Mol Imaging* 2007;34:532–40.
- [16] Dice LR. Measures of the amount of ecologic association between species. *Ecology* 1945;26:297–302.
- [17] Gregory R, Partridge M, Flower MA. Performance evaluation of the Philips “Gemini” PET/CT system. *IEEE Trans Nuclear Sci* 2006;53:93–101.
- [18] Teräs M, Tolvanen T, Johansson JJ, Williams JJ, Knuuti J. Performance of the new generation of whole-body PET/CT scanners: discovery STE and Discovery VCT. *Eur J Nucl Med Mol Imaging* 2007;34:1683–92.
- [19] Geworski L, Knoop BO, de Cabrejas ML, Knapp WH, Munz DL. Recovery correction for quantitation in emission tomography: a feasibility study. *Eur J Nucl Med* 2000;27:161–9.
- [20] Reader AJ. The promise of new PET image reconstruction. *Phys Med* 2008;24: 49–56.
- [21] Daisne JF, Duprez T, Weynand B, Lonnew M, Hamoir M, Reyckler H, et al. Tumor volume in pharyngolaryngeal squamous cell carcinoma: comparison at CT, MR imaging, and FDG-PET and validation with surgical specimen. *Radiology* 2004;233:93–100.
- [22] Geets X, Tomsej M, Lee JA, Duprez T, Coche E, Cosnard G, et al. Adaptive biological image-guided IMRT with anatomic and functional imaging in pharyngo-laryngeal tumors: impact on target volume delineation and dose distribution using helical tomotherapy. *Radiother Oncol* 2007;85:105–15.
- [23] Hanahan D, Weinberg RA. The hallmarks of cancer. *Cell* 2000;100:57–70.